Biases in Shortwave Column Absorption in the Presence of Fractal Clouds

ALEXANDER MARSHAK,* ANTHONY DAVIS,+ WARREN WISCOMBE, WILLIAM RIDGWAY,# AND ROBERT CAHALAN

Climate and Radiation Branch, NASA/Goddard Space Flight Center, Greenbelt, Maryland

(Manuscript received 1 January 1997, in final form 24 June 1997)

ABSTRACT

In this paper, the effect of cloud structure on column absorption by water vapor is investigated. Radiative fluxes above and below horizontally inhomogeneous liquid water clouds are computed using an efficient Monte Carlo technique, the independent pixel approximation, and plane-parallel theory. Cloud inhomogeneity is simulated by two related fractal models that use bounded cascades for the horizontal distribution of optical depth. The first (''clumpy'') model has constant cloud top and base, hence a constant geometrical thickness but varying extinction; the second (''bumpy'') model has constant extinction and cloud base, hence variable cloud-top and geometrical thickness. The spectral range between 0.9 and 1.0 μm (with strong water vapor absorption and negligible cloud liquid water absorption) is selected for a detailed study, not only of domain-averaged quantities, but also radiation fields. Column-absorption fields are calculated as the difference between the two net fluxes above and below clouds. It is shown that 1) redistribution of cloud liquid water decreases column absorption, that is, plane-parallel absorption is larger than the independent pixel approximation one by 1%–3%; 2) 3D radiative effects enhance column absorption by about 0.6% for the clumpy model and 2% for the bumpy model, that is, Monte Carlo absorption is larger than independent pixel approximation absorption—this effect is most pronounced for the bumpy cloud model at solar zenith angle $\approx 45°$; and 3) plane-parallel absorption is larger than 3D Monte Carlo absorption for high solar elevations and nearly equal to it for low solar elevations. Thus, for extended clouds of thickness 1–2 km or less, in an important water vapor absorption band (0.94 μm), the authors do not find a significant enhancement of cloud absorption due to horizontal inhomogeneity.

1. Introduction

Cloud absorption is an extremely difficult quantity to measure. As a rule, it is inferred from the difference between satellite-based estimates of the net fluxes at the top of the atmosphere (TOA) and collocated ones at the surface (Cess et al. 1995; Ramanathan et al. 1995) or between two stacked aircraft at fixed altitudes below and above clouds (Ackerman and Cox 1981; Hayasaka et al. 1995; Pilewskie and Valero 1995). Even though the measurements of both upward and downward fluxes have a fairly good accuracy, absorption is highly sensitive to the uncertainties which affect each component (Fouquart et al. 1990). On the other hand, general circulation models (GCMs) treat clouds as idealized horizontally homogeneous slabs with, at best, a correction for cloud ''fraction,'' although recently, Tiedke (1996) extended the plane-parallel parameterization of the ECMWF model to accommodate subgrid variability of optical depth as suggested by Cahalan et al. (1994). Paraphrasing Stephens and Tsay (1990), it is fair to say that both measurements and modeling of cloud absorption have their problems and the comparison is, at least, inconsistent.

Nevertheless, many observational studies report larger absorption than is predicted by models [see Reynolds et al. (1975); Stephens (1978a,b); Cess et al. (1995, 1996); Pilewskie and Valero (1995); Arking (1996); Li et al. (1997); and many others]. In situ measurements of single-scattering albedo (King et al. 1990) as well as plane-parallel computations forced to yield the same column absorption as observed (Chou et al. 1995), suggest that it is unlikely that the uncertainties in cloud microphysical properties are responsible for the discrepancy.

Recent simulations of broken cloudiness using stochastic radiative transfer (Byrne et al. 1996) and a detailed case study of a tropical cloud field (O'Hirok and Gautier 1998) indicate that at least part of the enhanced cloud absorption can be potentially explained by the inhomogeneous cloud structure. However, it is not yet

* Current affiliation: University of Maryland–Baltimore County, Baltimore, Maryland.
+ Current affiliation: Los Alamos National Laboratory, Los Alamos, New Mexico.
# Current affiliation: Space Application Corporation, Vienna, Virginia.

Corresponding author address: Dr. Alexander Marshak, NASA/GSFC, Code 913, Greenbelt, MD 20771.
E-mail: marshak@climate.gsfc.nasa.gov

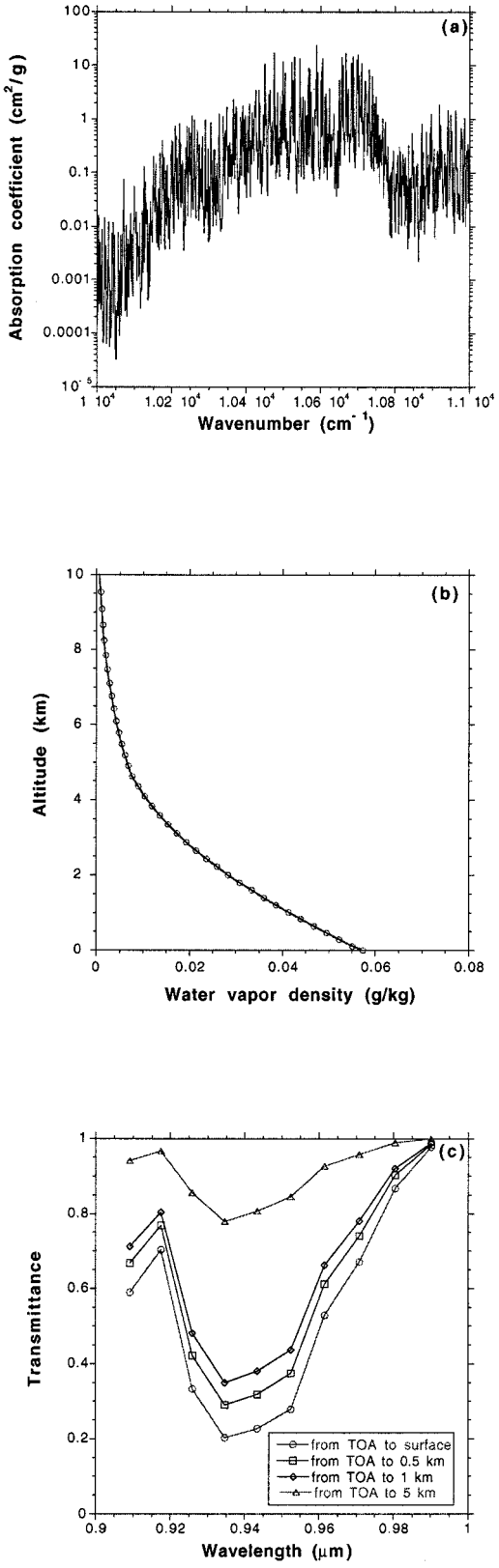

FIG. 1. Water vapor. (a) Spectral distribution of the lowest layer's absorption coefficient from 10 000 cm^{-1} (1 μm) to 11 000 cm^{-1} (0.91 μm) as computed line-by-line for reference conditions at 1000 mb and 294 K. The spectrum has been degraded to 1 cm^{-1} resolution. (b) Vertical distributions of water vapor density. (c) Water vapor transmission spectra for solar zenith angle $\theta_0 = 60°$. From the top: from TOA to 5 km, from TOA to 1 km, from TOA to 0.5 km, and, finally, from TOA to surface.

established that cloud inhomogeneity generally increases column absorption. Studies that consider only absorption by droplets (e.g., Stephens 1988; Harshvardhan et al. 1996; Barker 1996) indicate that the effect of finite clouds as well as cloud inhomogeneity *decreases* cloud absorption rather than increases it. So there is not a one-to-one correspondence between cloud morphology and absorption. Finally, it is hard to distinguish between enhanced absorption and variability of the cloud structure if spatial averaging is insufficient (Marshak et al. 1997a,b).

The goal of this study is to understand interdroplet cloud absorption in horizontally inhomogeneous clouds. In order to minimize the absorption by cloud drops, a spectral band around 0.94 μm with strong molecular and very weak liquid absorption has been chosen for detailed analysis. The 0.94-μm band has insignificant Rayleigh scattering and a large range of transmission (Figs. 1a,c). In addition, there is considerable incident flux, since it is near the peak of the solar spectrum. However, this is not a specific study of the 0.94-μm band per se, but rather our intention is to use that band to improve our understanding of shortwave absorption by water vapor. While a single wavelength is too specialized, integrating across the whole shortwave spectrum often gives little insight, since many diverse effects are lumped together.

In the present study, we estimate the effect of cloud inhomogeneity on ''apparent'' absorption (as a difference between two net fluxes simulated at fixed altitudes below and above clouds) as well as ''true'' absorption. The true column absorption is a combination of absorption by atmospheric gases, cloud liquid water, and aerosol. The only source of 3D effects is the horizontal distribution of cloud liquid water.

To distinguish between the effects of optical and geometrical inhomogeneities, two different but closely related fractal models of the distribution of cloud liquid water are used. Both have the same distribution of vertical optical depth, but the first one has constant cloud top and base but variable extinction (''flat'' or ''clumpy'' model), while the second one has variable cloud top with constant cloud base and extinction (''bumpy'' model).

Finally, three radiative transfer tools are applied to both cloud models. They are: 1) the ''weighted'' plane-parallel (PP) approach that distinguishes only between cloudy and clear pixels according to cloud fraction; 2) the independent pixel approximation (IPA) which ac-

←

TABLE 1. Solar irradiance values and characteristics of cloud liquid water scattering for each spectral interval within the 0.9–1.0-μm spectral band (Fouquart et al. 1991).

Wavenumber interval (cm^{-1})	Wavelength interval (μm)	Solar constant ($W\ m^{-2}$)	Cloud liquid water SSA, ϖ_o	Asymmetry factor, g
10000–10100	0.9901–1.0000	7.3159	0.9998	0.7983
10100–10200	0.9804–0.9901	7.3343	0.9998	0.7973
10200–10300	0.9709–0.9804	7.3474	0.9998	0.7958
10300–10400	0.9615–0.9709	7.3471	0.9998	0.7942
10400–10500	0.9524–0.9615	7.3499	0.9998	0.7959
10500–10600	0.9434–0.9524	7.3496	0.9998	0.7980
10600–10700	0.9346–0.9434	7.3508	0.9999	0.8002
10700–10800	0.9259–0.9346	7.3427	0.9999	0.8023
10800–10900	0.9174–0.9259	7.3277	0.9999	0.8043
10900–11000	0.9091–0.9174	7.3211	1.0000	0.8065

counts for the probability distribution of cloud optical depth but neglects net horizontal fluxes; and 3) the Monte Carlo (MC) method which accounts for the net horizontal fluxes by simulating the full 3D radiative transfer process.

The main original points to be discussed in this paper are

- change in column absorption due to redistribution of cloud liquid water
- change in column absorption due to horizontal fluxes
- effects of clumpiness versus bumpiness on cloud absorption
- effects of cloud fraction and solar zenith angle.

This paper is structured as follows. First, we describe our model atmosphere. Next, section 3 discusses the three radiative transfer techniques applied to the model atmosphere. We study the change in column absorption due to redistribution of cloud liquid water for clumpy and bumpy models. The effect of cloud fraction is discussed in section 4, while PP and IPA biases are defined and analyzed in section 5. Finally, section 6 summarizes our analysis. In addition, appendix A formally describes the effect of net horizontal fluxes, while in appendix B, the stability and reliability of our results are justified.

2. Model atmosphere

Our model atmosphere consists of 51 homogeneous layers defined by constant pressure increments of 20 mb (Ellingson et al. 1991). Two main components of the atmosphere are included: water vapor and clouds; we also had the option to add a climatological aerosol load and a reflecting surface.

a. Water vapor

In the spectral range 0.9–1.0 μm, water vapor is the only significant absorbing gas. Figure 1a shows spectral absorption of water vapor for the midlatitude summer model in 0.91–1.0 μm, while the vertical profile of water vapor density is plotted in Fig. 1b. This band contains both strong and weak water vapor absorption; the whole clear atmospheric column transmits only about 20% around 0.94 μm but nearly 98% around 1.0 μm for solar zenith angle $\theta_0 = 60°$ (Fig. 1c). For the same θ_0, the clear-sky column absorption in the spectral interval 0.91–1.0 μm is $\approx$17 W m^{-2}, which is $\approx$46% of the normal incident solar flux ($\approx$37 W m^{-2}); for reference, it is $\approx$11 W m^{-2} between two altitudes of interest (5 and 0.5 km) in our two-aircraft simulations. These numbers come from radiative transfer models; there is no independent confirmation from measurements, but they are likely good ballpark figures.

The water vapor transmission function $t(l)$ for path length l is calculated separately for each of ten 100 cm^{-1} bands covering 10 000–11 000 cm^{-1} using an exponential sumfit approximation:

$$t(l) = \sum_{i=1}^{n} a_i \exp\left(-\sum_{j=1}^{m} k_{ij} l_j\right),$$

$$\left(0 \le a_i \le 1,\ \sum_{i=1}^{n} a_i = 1,\ k_{ij} \ge 0,\ \sum_{j=1}^{m} l_j = l\right),$$

with $n = 8$ and $m = 51$. The absorption coefficients k_{ij} and the weights a_i were calculated using a multilayer correlated k-method (Lacis and Oinas 1991). Absorption spectra were computed line-by-line (Fig. 1a) for each of the 51 layers, then reduced to cumulative k-distribution functions independently computed for each layer. The k-values were binned from the cumulative distribution function using a set of logarithmically spaced absorption bin boundaries defined on the lowest layer. (For the purpose of reproducibility, the coefficients k_{ij} and the weights a_i for all 10 bins can be found in the anonymous directory /user/ftp/pub/marshak/K_distr on the server climate.gsfc.nasa.gov).

Figure 1c illustrates four transmission spectra calculated for the water vapor profile from Fig. 1b for solar zenith angle $\theta_0 = 60°$. From the top: transmission from TOA to 5 km (the upper aircraft), to 1.0 km [cloud bottom (see section 2c)], to 0.5 km (the lower aircraft) and to the surface. Points indicate ten 100 cm^{-1} bands (Table 1).

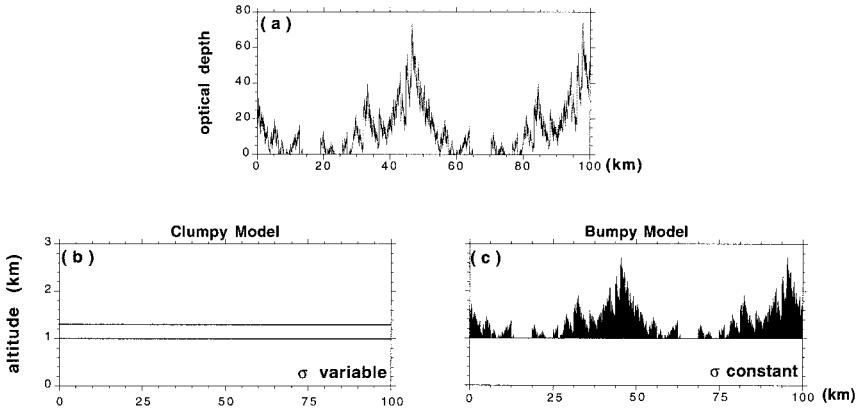

FIG. 2. Cloud models. (a) Horizontal distribution of optical depth, the same for both models. (b) Horizontal distribution of cloud height for clumpy model. Constant cloud top and cloud base; thus, $\sigma = \tau/h$ is variable. (c) Horizontal distribution of cloud top for bumpy model. Having σ constant, $h_{\text{top}} = h_{\text{base}} + \tau/\sigma$. To emphasize periodical boundary conditions, two basic cells of ≈50 km are plotted next to each other.

b. Clouds

The only source of horizontal variability in our atmospheric model is clouds. To simulate the horizontal distribution of cloud optical depth, τ, we use a simple three-parameter fractal model called a ''bounded cascade'' (Cahalan et al. 1994) for which

$$0 < \tau_{\min} \le \tau \le \tau_{\max} < \langle\tau\rangle \exp\left(\frac{1 - 2p}{1 - 2^{-H}}\right) < \infty, \quad (2)$$

where $\langle\cdot\rangle$ indicates domain average. Parameter p controls the variance-to-mean ratio of cloud liquid water while H determines its scaling behavior (Marshak et al. 1994). In this study, the cascade parameters are fixed at $\langle\tau\rangle = 13$, $p = 0.35$, and $H = 0.38$. According to the analyses of Cahalan and Snider (1989) and Cahalan (1994), these values provide the best fit to the diurnal average liquid water path (LWP) distribution in California marine Sc. The average optical depth corresponds to $\langle\text{LWP}\rangle = 90$ g m^{-2} assuming a cloud drop effective radius $\langle r_e\rangle = 10$ μm. The typical marine Sc cloud thickness $h = 300$ m. This gives a mean extinction coefficient $\langle\sigma\rangle = \langle\tau\rangle/h = 43$ km^{-1}.

Depending on which of the two parameters, physical cloud thickness h and extinction coefficient σ is set constant; we distinguish between two models of the horizontal distribution of cloud optical depth:

- ''Clumpy fractal'' means σ variable, h constant (both cloud top and cloud base are horizontal planes); assuming σ has no vertical variation, we have $\sigma = \tau/h$.
- ''Bumpy fractal'' means h variable, σ constant; h is therefore proportional to τ with $\langle h\rangle = 300$ m and, for simplicity, we keep cloud base fixed and vary only cloud top.

TABLE 2. Cloud fractions. $\langle\tau_{\text{cloudy}}\rangle$ is defined in (5); parameters a and b are defined implicitly in (3).

N	$\langle\tau_{\text{cloudy}}\rangle$	$\tau_{\max}$	a	b
1.000	13.00	39.3	0.0	1.0
0.930	13.98	59.1	5.6	1.8
0.777	16.73	74.4	7.9	2.4
0.685	18.98	85.1	9.1	2.8

Examples of the two contrasting models are shown in Fig. 2.

Finally, in addition to cloud inner structure simulated with the bounded cascade model, we supplement the cloud structure with gaps. For simplicity, and lacking any good theory on cloud gappiness, we subtract a constant value $a > \tau_{\min}$ from the bounded-model optical depth curve $\tau_{\text{unbroken}}(x)$ and set negative values to zero (see Barker and Davies 1992 for discussion and justification). This, however, does not conserve liquid water; so in order to restore the liquid water to its former value, we multiply the resulting optical depth curve by another constant $b > 1$. As a result, we have

$$\tau_{\text{broken}}(x) = b_{\max}[\tau_{\text{unbroken}}(x) - a, 0]. \quad (3)$$

Constants a and b can be uniquely derived from the desired fractional cloudiness N and three parameters of the bounded model: $\langle\tau\rangle$, p, and H. [The nonlinear transformation (3) perturbs the scaling properties of the original field but, for the purposes of this paper, it is more important to study the effect of broken cloudiness than to keep cloud optical depth strictly scale-invariant.] Figure 2 gives an example for both types of cloud model with fractional cloudiness $N = 0.777$, corresponding to $a \approx 7.9$ and $b \approx 2.4$. For other cloud fractions see Table 2. Comparison of the gap distribution in this model to observations is left to the future (see Cahalan et al. 1995 for discussion of gap distribution in FIRE and ASTEX).

Different values of single scattering albedo ϖ_0 and asymmetry factor g, given in Table 1, are used for each 100 cm^{-1} spectral interval. The Henyey–Greenstein

TABLE 3. PP and 1PA reflectance, transmittance, and resulting absorption for a clumpy cloud model with only four pixels. Sun in zenith, $\langle\tau_{\text{cloudy}}\rangle = \langle\tau\rangle/N$, with $\langle\tau\rangle = 13$ and $N = 0.75$.

	τ	R	T	A
Clear	0.0	0.000	0.752	0.248
Cloudy	17.3	0.432	0.240	0.328
Average	13.0	0.384	0.296	0.320
PP [(8)]		0.324	0.368	0.308
IPA [(11)]		0.296	0.400	0.304

phase function model is used for simplicity. Note that in the interval between 10000 and 11000 cm^{-1}, cloud liquid water absorbs very weakly; the smallest $\varpi_0 = 0.9998$. Assuming that for $\langle\tau\rangle = 13$, the average number of scatterings is 30 [20 for reflected photons and 40 for transmitted ones (Marshak et al. 1995)], we have $\varpi_0^{30} \approx 0.994$; that is, less than 1% of the radiant energy is absorbed by liquid water.

3. Numerical radiative transfer: Tools and results

In this section we discuss and compare the three radiative transfer methods employed in this study: the ''weighted'' plane-parallel approximation, the independent pixel approximation, and Monte Carlo simulation. Using these methods, we compute downward and upward fluxes at 5 km (above clouds) and at 0.5 km (below clouds).

The reflectance R, transmittance T, and absorptance A are defined as

$$R = F_{\text{u}}^{\text{a}}/F_{\text{d}}^{\text{a}}, \tag{4a}$$

$$T = F_{\text{d}}^{\text{b}}/F_{\text{d}}^{\text{a}}, \quad \text{and} \tag{4b}$$

$$A = [(F_{\text{d}}^{\text{a}} - F_{\text{u}}^{\text{a}}) - (F_{\text{d}}^{\text{b}} - F_{\text{u}}^{\text{b}})]/F_{\text{d}}^{\text{a}}, \tag{4c}$$

where F is radiative flux, suffixes ''d'' and ''u'' denote downward and upward, and suffixes ''a'' and ''b'' denote above and below cloud.

a. Plane-parallel approximation

For unbroken clouds, the results of the PP approximation is straightforward: use mean optical depth $\langle\tau\rangle$ and mean geometrical thickness $\langle h\rangle$ in a standard PP model. Plane-parallel results for clumpy and bumpy models differ only for broken clouds ($N < 1$). Indeed, the domain average

$$\langle\tau\rangle = N\langle\tau_{\text{cloudy}}\rangle = N\langle\sigma_{\text{cloudy}}h_{\text{cloudy}}\rangle \tag{5}$$

for both models. However, since $\{\langle\tau_{\text{cloudy}}\rangle\}_{\text{clumpy}} = \{\langle\tau_{\text{cloudy}}\rangle\}_{\text{bumpy}}$, we have

$$\{\langle\sigma_{\text{cloudy}}\rangle h_{\text{cloudy}}\}_{\text{clumpy}} = \{\sigma_{\text{cloudy}}\langle h_{\text{cloudy}}\rangle\}_{\text{bumpy}}; \tag{6}$$

thus,

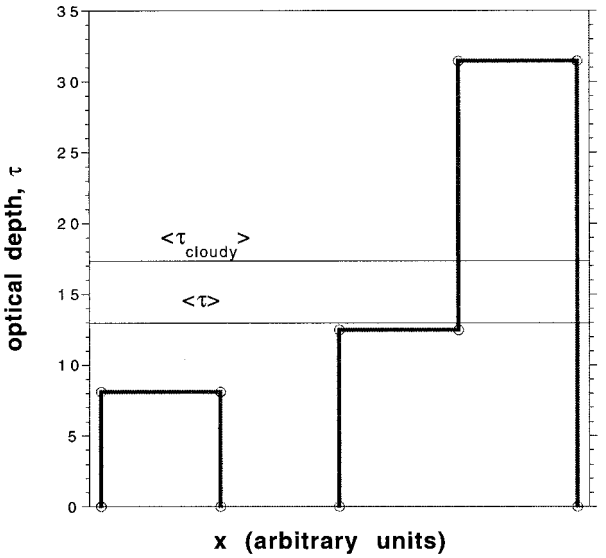

FIG. 3. Clumpy cloud model with only four pixels. $\langle\tau_{\text{cloudy}}\rangle$ is averaged over three cloudy pixels and $\langle\tau\rangle$ is averaged over all four pixels.

$$\{\langle\sigma_{\text{cloudy}}\rangle\}_{\text{clumpy}} = \frac{\{\langle h_{\text{cloudy}}\rangle\}_{\text{bumpy}}}{\{h_{\text{cloudy}}\}_{\text{clumpy}}}\{\sigma_{\text{cloudy}}\}_{\text{bumpy}} = \frac{1}{N}\{\sigma_{\text{cloudy}}\}_{\text{bumpy}}. \tag{7}$$

In other words, the mean extinction of cloudy pixels in the clumpy model is $1/N$ times larger than the extinction in the bumpy one.

Finally, PP fluxes are defined as the weighted sum of clear and cloudy fractions; that is,

$$F_{\text{PP}} = NF_{\text{cloudy}} + (1 - N)F_{\text{clear}}. \tag{8}$$

Table 3 shows the results of PP calculations for the horizontally inhomogeneous clouds plotted in Fig. 3 (clumpy model with four pixels); illumination is from the zenith. Out of four pixels, one represents clear sky; thus, cloud fraction $N = 0.75$. This yields $\langle\tau_{\text{cloudy}}\rangle = \langle\tau\rangle/N = 17.3$, which is used to calculate F_{cloudy}. Note that here $F_{\text{u}}^{\text{b}} \equiv 0$ and $F_{\text{d}}^{\text{a}} \equiv 0.94$ independently of clouds. The overall PP fluxes are computed using (8).

Comparing two values of reflectance, R_{PP} and $R(\langle\tau\rangle)$, and two values of transmittance, T_{PP} and $T(\langle\tau\rangle)$ in Table 3, we see that

$$R_{\text{PP}} < R(\langle\tau\rangle), \tag{9a}$$

(i.e., inhomogeneous clouds are darker than their homogeneous counterparts) while

$$T_{\text{PP}} > T(\langle\tau\rangle). \tag{9b}$$

This is a direct consequence of Jensen's inequality (e.g., Polya and Szegö 1964):

$$\varphi\left(\sum_{i=1}^{n} p_i t_i\right)\begin{cases}\le \sum_{i=1}^{n} p_i\varphi(t_i), & \varphi\text{concave } (\varphi''\ge 0)\\ \ge \sum_{i=1}^{n} p_i\varphi(t_i), & \varphi\text{convex } (\varphi''\le 0),\end{cases} \tag{10a}$$

and

$$\sum_{i=1}^{n} p_i = 1, \qquad p_i \ge 0, \tag{10b}$$

where $t_1, t_2, \ldots, t_n$ are arbitrary points. Indeed, putting $n = 2$, $p_1 = 1 - N$, $p_2 = N$, $t_1 = 0$, $t_2 = \langle\tau_{\text{cloudy}}\rangle$, and remembering that R is a convex function of τ and T concave, (10a) applies and explains inequalities (9a)–(9b).

b. Independent pixel approximation

Independent pixel approximation is just an extension of the idea of making the binary decision for each pixel (cloudy or clear) to attaching a number to each pixel (its optical depth τ_i, $i = 1, \ldots, n_p$). The domain-averaged flux within the IPA for clouds with n_p pixels is

$$F_{\text{IPA}} = \frac{1}{n_p}\sum_{i=1}^{n_p} F(\tau_i). \tag{11}$$

This is a generalization of the two-term sum for the PP approximation in (8).

1) IPA versus PP

Table 3 provides the domain-averaged IPA values for R, T, and A. We can see that for reflectance,

$$R_{\text{IPA}} < R_{\text{PP}} < R(\langle\tau\rangle), \tag{12a}$$

while for transmittance,

$$T_{\text{IPA}} > T_{\text{PP}} > T(\langle\tau\rangle). \tag{12b}$$

These inequalities are well known and they follow immediately from (10a,b) with $n = n_p$ and $p_i = 1/n_p$, where n_p is the total number of pixels.

We cannot derive similar inequalities to (12a) or (12b) for absorption; being the difference of convex and concave functions, A is, in general, neither. The dependence of A on τ is affected by many factors including illumination conditions, phase function, single scattering albedo, and distribution of cloud liquid water and water vapor. However, for the spectral range around 0.94 μm and our atmospheric model, we found that (Tables 3 and 4)

$$A_{\text{IPA}} < A_{\text{PP}} < A(\langle\tau\rangle), \tag{12c}$$

which is a direct consequence from the convexity of A plotted in Fig. 4a for both clumpy and bumpy models.

2) Clumpy versus bumpy cloud models

We now compare results of the IPA for clumpy and bumpy models. Figure 4b shows both R and T plotted against optical depth. It is clearly seen that while transmittances are similar, the reflectance of the bumpy model substantially exceeds its counterpart for the clumpy model, at least for large values of τ.

TABLE 4. Results of PP, IPA, and MC calculations for both clumpy and bumpy model. Cloud fraction $N = 0.777$ and solar zenith angle $\theta_0 = 60°$. Note that for PP calculations, $h_{\text{clumpy}} = 0.3$ km, while $h_{\text{bumpy}} = 0.3/N = 0.386$ km.

		PP		IPA		MC	
F	$F(\langle\tau\rangle)$	Clumpy	Bumpy	Clumpy	Bumpy	Clumpy	Bumpy
R	0.450	0.373	0.376	0.324	0.332	0.334	0.333
T	0.191	0.273	0.273	0.323	0.324	0.312	0.316
A	0.359	0.354	0.351	0.353	0.344	0.354	0.351

To emphasize this, in Fig. 4c, two narrow (100 cm^{-1}) spectral intervals are plotted separately. One (around 0.99 μm) is the least absorptive, while the other (around 0.94 μm) is the most absorptive. In the least absorptive interval there is almost no difference between bumpy and clumpy models, while in the most absorptive one, the reflectance difference is pronounced starting from $\tau \approx 20$. For transmitted photons, the difference is very small for both spectral intervals.

To summarize, in the frame of IPA,

$$R_{\text{IPA}}^{\text{clumpy}} < R_{\text{IPA}}^{\text{bumpy}} \quad \text{and} \tag{13a}$$

$$T_{\text{IPA}}^{\text{clumpy}} \approx T_{\text{IPA}}^{\text{bumpy}}; \tag{13b}$$

thus,

$$A_{\text{IPA}}^{\text{clumpy}} > A_{\text{IPA}}^{\text{bumpy}}. \tag{13c}$$

The validity of (13c) is illustrated in Fig. 4a.

To explain (13a)–(13b), first note that, in the narrow band around 0.94 μm, photons are almost exclusively absorbed by water vapor. Thus, to estimate column absorption, one has to ''measure'' photon pathlengths in both models. Based on the diffusion approximation (e.g., van de Hulst 1980), it can be shown that for large optical thicknesses, the average total pathlength for reflected photons is longer for the clumpy model than for the bumpy one and vice versa for transmitted photons. These results are independent of the vertical distribution of water vapor. However, embedded in the midlatitude summer model of water vapor, photons traveling the same pathlength in lower levels (clumpy model) are more likely absorbed by water vapor than those traveling in upper levels (bumpy model). This explains why in Figs. 4b and 4c the large-τ reflectance of the bumpy model substantially exceeds that of the flat clumpy model (13a), but the flat model's transmittance is only slightly larger than for the bumpy one (13b).

In short, 3D cloud inhomogeneity treated on a per-pixel basis with 1D radiative transfer decreases column absorption in comparison to PP results. The values of column absorption together with reflectance and transmittance are summarized in Table 4 for cloud fraction $N = 0.777$ and solar zenith angle $\theta_0 = 60°$.

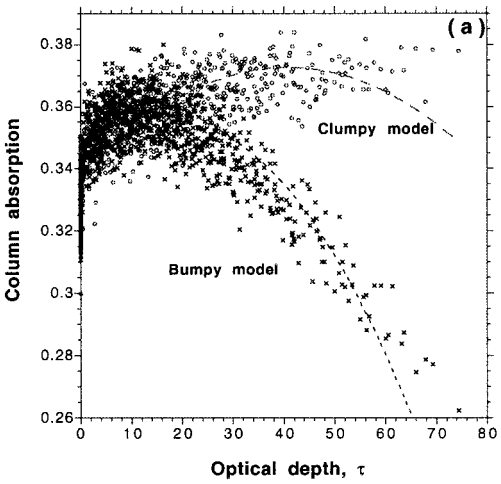

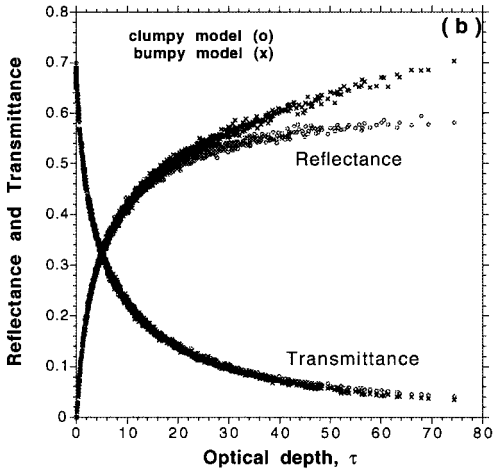

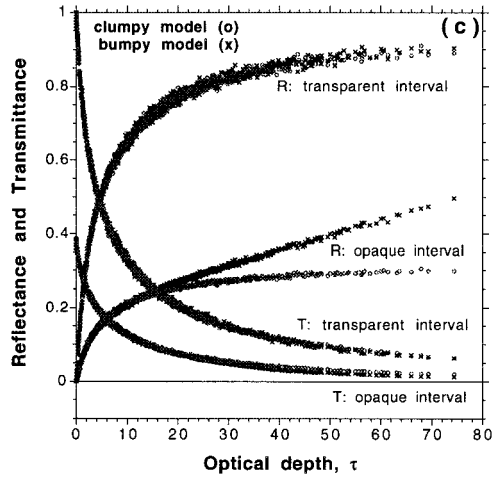

Finally, in contrast to PP, the IPA treats properly the full horizontal distribution of cloud optical depth. However, it ignores all interpixel connections and exchanges by considering each pixel as an independent plane-parallel stratified medium. These net horizontal fluxes affect our definition of column absorption by introducing a term that has no counterpart in the IPA. In the next section, we account for horizontal fluxes by using the fully 3D numerical technique, Monte Carlo simulation.

c. Monte Carlo method

To simulate two aircraft measurements below and above clouds, we use a ''forward'' Monte Carlo method. Technical questions about pixel size, number of photons, accuracy of MC, substitution of a ''forward'' for a ''backward'' scheme, and realization dependence are discussed in appendix B.

1) ''APPARENT'' VERSUS ''TRUE'' COLUMN ABSORPTION FIELDS

In contrast with 1D radiative transfer, the 3D theory can distinguish between ''apparent'' absorption A^*, the observable quantity defined as the difference between two net fluxes at different levels in the atmosphere, and ''inherent'' or ''true'' column absorption A. The latter quantity can only be computed.

Let us assume that cloud properties vary only in the x-direction horizontally. Then, using the continuity equation for radiant energy, one can show (appendix A) that the apparent A^* absorption at point x is a sum of two terms (Titov 1998; Davis et al. 1997), namely

$$A^*(x) = H(x) + A(x). \tag{14}$$

The first term, $H(x)$, describes the convergence/divergence pattern of the horizontal flow of photons, while the second term, $A(x)$, is the ''true'' absorption that contributes to heating rate in the column between two aircraft. On average,

$$\langle H \rangle = 0; \tag{15}$$

thus, the domain-averaged apparent absorption is equal to the true column absorption,

←

FIG. 4. IPA reflectance, transmittance, and absorption vs optical depth for both bumpy and clumpy models. Cloud fraction $N = 0.777$, solar zenith angle $\theta_0 = 60°$. (a) Column absorption. Two polynomial fits: $-2\ 10^{-5}\ \tau^2 + 2\ 10^{-3}\ \tau + 0.3$ (clumpy model) and $-4\ 10^{-5}\ \tau^2 + 2\ 10^{-3}\ \tau + 0.3$ (bumpy model) are added for the illustration of convexity. (b) Reflectance and transmittance. For the domain-averaged values, see Table 4. (c) Reflectance and transmittance for two narrow bands. Two spectral intervals around 0.99 μm (least absorptive) and 0.94 μm (most absorptive). The thickness of the curves characterizes the level of noise (see appendix B).

$$\langle A^* \rangle = \langle A \rangle. \tag{16}$$

For a case study with $A(x) \equiv 0$ and $A^*(x) \neq 0$, we refer to Davis et al. (1997). In this study, we have $A(x) \geq 0$, whereas $A^*(x)$ can have any sign.

2) Comparison with IPA using the bumpy cloud model

Figure 5a shows IPA and MC results of reflectance and transmittance measured at 5 and 0.5 km, respectively. The horizontal distribution of optical depth is added for convenient reference. We see that while there is a strong correlation between the two transmittance fields, the small-scale behavior of reflectance fields is entirely different. The upward fluxes, ''measured'' more than 2 km above the highest cloud pixel (bumpy model), are smoothed by contributions from at least 140 pixels on average; thus, only large-scale variability of optical depth affects the MC upward fluxes (Barker 1995). On the contrary, the IPA reflected fluxes follow the variability of cloud optical depth on a pixel-by-pixel basis. Averaging over the whole domain (≈50 km), however, cancels most of the discrepancies between IPA and MC upward fluxes; the domain-average bias for the bumpy cloud model is negligible (Table 4).

The case of transmittance fields is more intriguing. First, there is a shift between IPA- and MC-computed spikes (e.g., the one around $x = 5$ km). The reason for the shift is trivial and is due to the 60° sun angle and the direct radiation ''measured'' 0.5 km below cloud bottom. However, most MC spikes are much stronger than the IPA ones (see spikes around 10, 20, 26, and 30 km, etc.). All these spikes are about 1 km from the right edge of the cloud gaps and indicate bright spots in the local broken-cloudy sky.

On average, however, IPA transmittance exceeds its MC counterpart, at least for low sun (Table 4). This is because some photons are trapped between two clouds, thus accumulating path and increasing absorption. To illustrate this, the apparent column absorption $A^*(x)$ between two levels, above and below clouds, is plotted in Fig. 5b. Since the upward flux above clouds is a smooth curve (Fig. 5a), the fluctuations of $A^*(x)$ follows those of $T(x)$. As a result, near cloud edges (or near large fluctuations of the optical depth) apparent MC absorption exceeds IPA by factor of 2, while at low τ, there is a deficit with respect to IPA (including going negative). Finally, in Figs. 6a–c, reflectance, transmittance, and resulting absorption for both MC and IPA are plotted versus optical depth. We see that for large τ, the range is between 0.2 and 0.5 for MC absorption, while for small τ (i.e., near cloud edges), the range is much broader: from -0.4 (locally negative absorption!) to 0.7.

Negative absorption (which is a counterpart of transmission exceeding unity) has frequently been observed (Herman and Goody 1976; Fouquart et al. 1990); some investigations have discarded such data as spurious. If one rejects data points with negative absorptions (≈7%–8% of all points), wrongly considering them as unphysical, the domain-average absorption will be ≈10% higher than its ''true'' value. This alone yields a spurious 1–2 W m^{-2} absorption enhancement within our narrow band, corresponding roughly to 10–20 W m^{-2} for the entire solar spectrum.

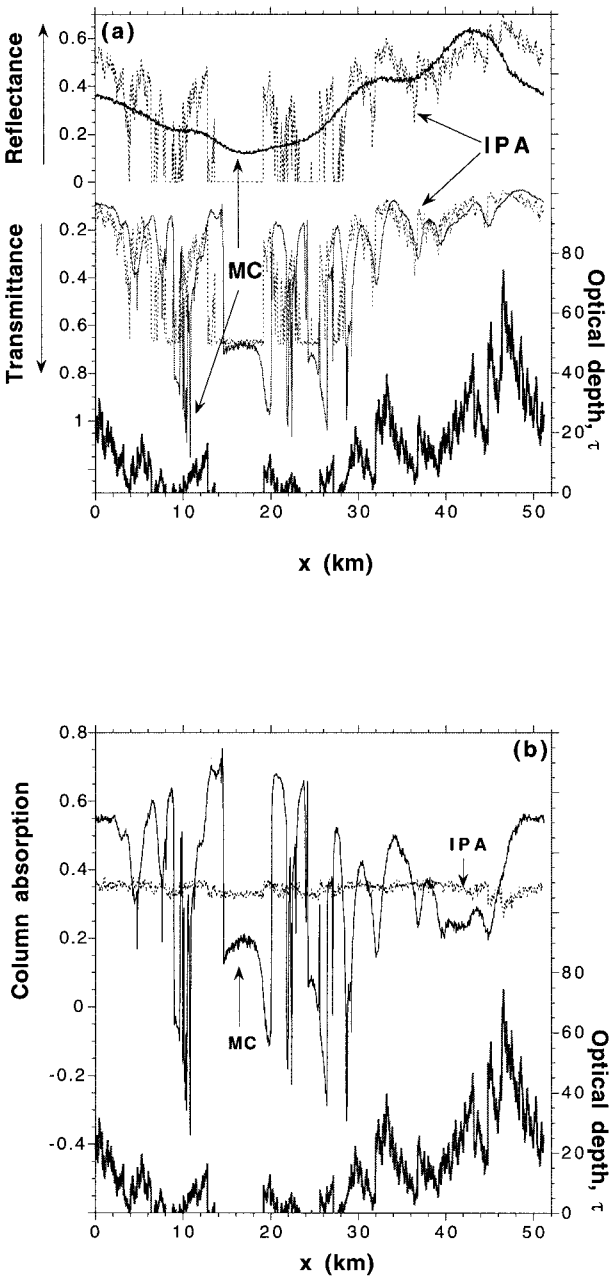

FIG. 5. Reflectance, transmittance, and column absorption fields computed by IPA and MC. Bumpy model with $N = 0.777$, solar zenith angle $\theta_0 = 60°$, and illumination from the left. Optical depth distribution $\tau(x)$ is added for reference. (a) $R(x)$ and $T(x)$ vs x. (b) *Apparent* column absorption $A^*(x)$ vs x for MC and *true* column absorption $A(x)$ vs x for IPA.

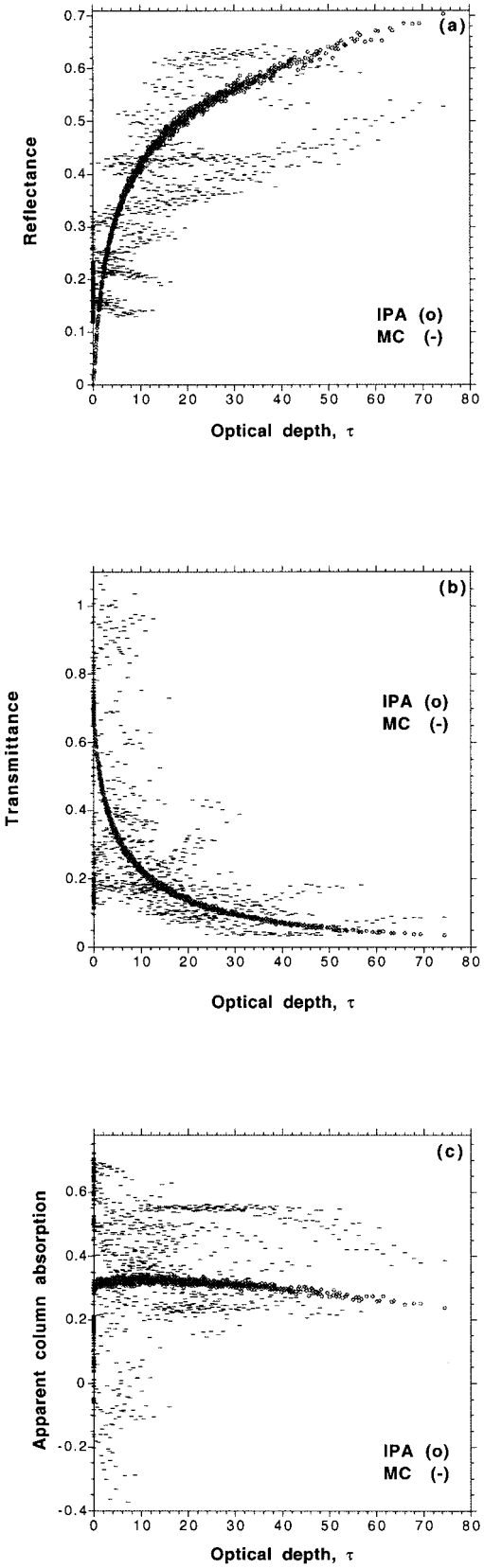

FIG. 6. Reflectance, transmittance, and corresponding apparent column absorption from Fig. 5 plotted vs τ. All parameters are as in Fig. 5. (a) Reflectance. (b) Transmittance. (c) Absorptance.

3) Comparison between clumpy and bumpy models

We now compare the MC fluxes for both bumpy and clumpy models. In the case of IPA, $R_{\mathrm{IPA}}^{\mathrm{clumpy}} < R_{\mathrm{IPA}}^{\mathrm{bumpy}}$ while $T_{\mathrm{IPA}}^{\mathrm{clumpy}} \approx T_{\mathrm{IPA}}^{\mathrm{bumpy}}$. As a result, $A_{\mathrm{IPA}}^{\mathrm{clumpy}} > A_{\mathrm{IPA}}^{\mathrm{bumpy}}$ (see section 3b and Table 4).

Figure 7 illustrates reflectance and transmittance for both models at $\theta_0 = 60°$. As for reflectance, there are two competing processes: on one hand, the reflected photons have longer paths in the flat model, forcing $R^{\mathrm{clumpy}} < R^{\mathrm{bumpy}}$ (IPA effect); on the other hand, in the bumpy model, shadowing forces some photons to bounce back into clouds, forcing $R^{\mathrm{clumpy}} > R^{\mathrm{bumpy}}$ (MC effect). As a result, for large τ we have $R^{\mathrm{clumpy}} < R^{\mathrm{bumpy}}$ (see bump at $x \approx 42$ km), for $\tau \approx \langle\tau\rangle$ both models give similar reflectances ($x \approx 20$ km), and for other optical depths, $R^{\mathrm{clumpy}} > R^{\mathrm{bumpy}}$ (e.g., $x < 10$ km and $x > 45$ km). In contrast with the IPA, the domain-averaged reflectances show that an MC effect slightly dominates, giving $R^{\mathrm{clumpy}} > R^{\mathrm{bumpy}}$ (Table 4).

The flux transmitted through the clumpy cloud looks smoother than the one transmitted through the bumpy cloud. Some spikes of the bumpy model transmittance are no longer there for a constant h (thus variable σ). For example, the spike at $x \approx 5$ km that corresponds to the gap in $\tau(x)$ at $x \approx 4$ km is canceled because of the small extinction around this gap that allows photons to proceed farther (in case of bumpy model, $\sigma \approx 43$ km^{-1} is fixed; this forces photons to bounce back and hence to increase cloud-edge transmittance). As a result, $T^{\mathrm{clumpy}} < T^{\mathrm{bumpy}}$ (Table 4).

As shown in section 3b(2), $A_{\mathrm{IPA}}^{\mathrm{clumpy}}$ exceeds $A_{\mathrm{IPA}}^{\mathrm{bumpy}}$. This means that for the same amount of liquid water, if the horizontal fluxes are not accounted for [i.e., $H(x) \equiv 0$], then the increase in cloud geometrical thickness decreases absorptance. However, this is no longer true for the MC column absorption that shows less difference between clumpy and bumpy models for all solar angles. As a result, the IPA deficit of absorption in the bumpy model is compensated, and MC column absorption ends up being only weakly dependent on the cloud model.

Finally, since

$$(A_{\mathrm{MC}}^{\mathrm{clumpy}} - A_{\mathrm{IPA}}^{\mathrm{clumpy}}) < (A_{\mathrm{MC}}^{\mathrm{bumpy}} - A_{\mathrm{IPA}}^{\mathrm{bumpy}}) \qquad (17)$$

for domain averages, the effect of horizontal fluxes on column absorption is more pronounced in the case of the bumpy model than in the case of the clumpy one. This is true for all solar angles and is not much affected by the direct-beam shadowing from neighboring columns.

←

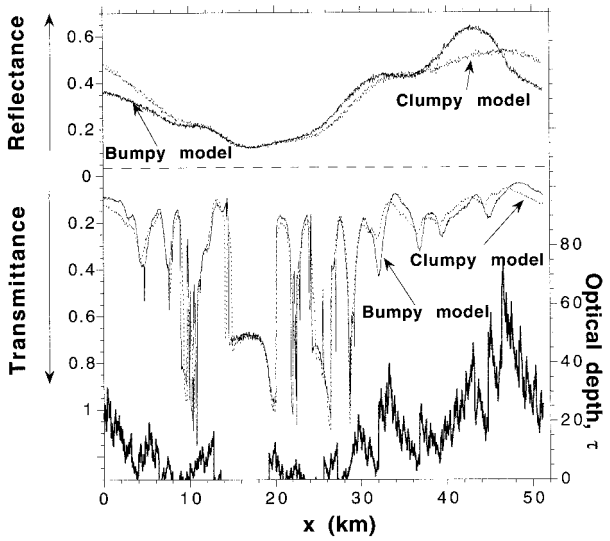

FIG. 7. MC reflectance and transmittance for clumpy and bumpy models. Cloud fraction $N = 0.777$ and solar zenith angle $\theta_0 = 60°$.

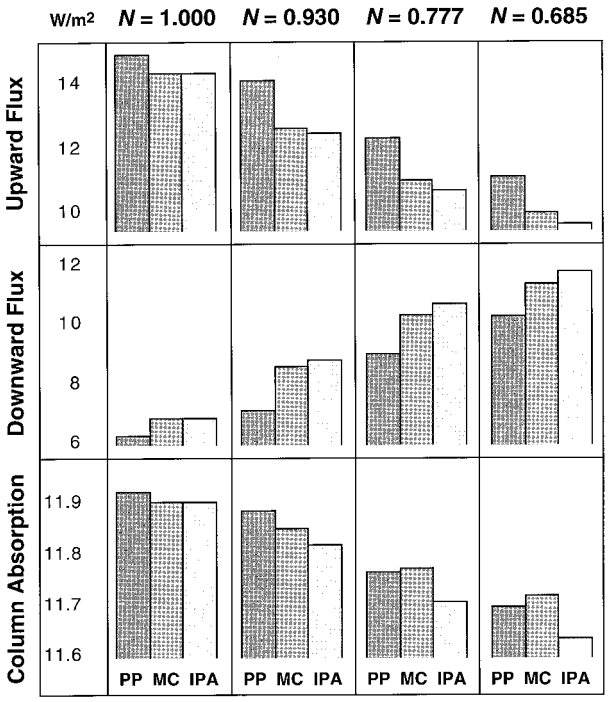

FIG. 8. The effect of cloud fraction. Domain-averaged upward flux, downward flux, and resulting column absorption are plotted for four cloud fractions (Table 2) and three radiative transfer models: PP, MC, and IPA. Flat/clumpy cloud model, solar zenith angle $\theta_0 = 60°$. Physical units of W m^{-2} are used; reflectance, transmittance, and absorption defined in (4a)–(4c) are multiplied by a factor $F_d^a(\theta_0)F_0(\lambda)\cos\theta_0$, where $F_0(\lambda)$ is the solar constant (see Table 1) and $F_d^a(60°) = 0.907$ is the normalized downward flux above clouds but below a small amount of water vapor.

4. Cloud-fraction effect

In this section we compare results for different cloud fraction N; the same total liquid water is used in all cases. With more gaps, redistribution of cloud liquid water increases optical depth of cloudy sky (see Table 2).

For $\theta_0 = 60°$, Fig. 8 shows the domain-averaged up- and downward fluxes together with the column absorption for different cloud fractions computed using all three radiative transfer tools: PP, IPA, and MC. Obviously, with the decrease of cloud fraction, reflectance decreases, while transmittance increases for all three models. The decrease in absorption is also easy to understand in the framework of the IPA, since clear-sky pixels absorb less than their cloudy counterparts. What is less obvious is that MC results for reflectance and transmittance are between PP and IPA results for any cloud fraction N. In other words, for $\theta_0 = 60°$,

$$R_{\mathrm{IPA}} < R_{\mathrm{MC}} < R_{\mathrm{PP}} \tag{18a}$$

and

$$T_{\mathrm{IPA}} > T_{\mathrm{MC}} > T_{\mathrm{PP}}. \tag{18b}$$

A key ingredient here is slant illumination and thus direct-beam shadowing from neighboring columns. Overhead sun gives the opposite order for MC and IPA in (18a) and (18b) (for discussion, see Davis et al. 1991).

The difference between IPA and MC—the so-called IPA bias (see next section)—increases with the decrease of cloud fraction, not only for reflectance and transmittance but also for column absorption. The overcast case ($N = 1$) does not produce any visible differences between IPA and MC, at least for clumpy clouds. Inequalities (18a) and (18b) are still valid (the difference is in the third digit), but the resulting domain-averaged column absorption is the same for both IPA and MC. In our fractal models, increasing gappiness not only increases the clear-sky fraction (like in the PP case) but also increases the number of gaps, hence the number of cloud edges and the effect of horizontal fluxes. With more gaps, more photons are trapped between cloudy pixels, thus accumulating water vapor absorption; as a result, $A_{\mathrm{MC}} > A_{\mathrm{IPA}}$.

Figure 9 illustrates the results of MC for each of 10 narrow bands. We see that for the transparent band (around 0.99 μm), the deficit of reflected photons for broken clouds (Fig. 9a) is fully compensated by the transmitted photons (Fig. 9b); as a result, column absorption (lower part of Fig. 9c) is almost insensitive to cloud cover. On the other hand, for the ''opaque'' bands (around 0.94), the absolute difference between downward fluxes exceeds that of upward fluxes. As a result, column absorption for overcast sky exceeds those of broken clouds. This is valid for all narrow bands, however, the most pronounced for almost opaque bands from 0.93 to 0.96 μm (Fig. 9c).

5. Biases

It is more convenient to deal not with absolute values of radiative fluxes for different models but with their

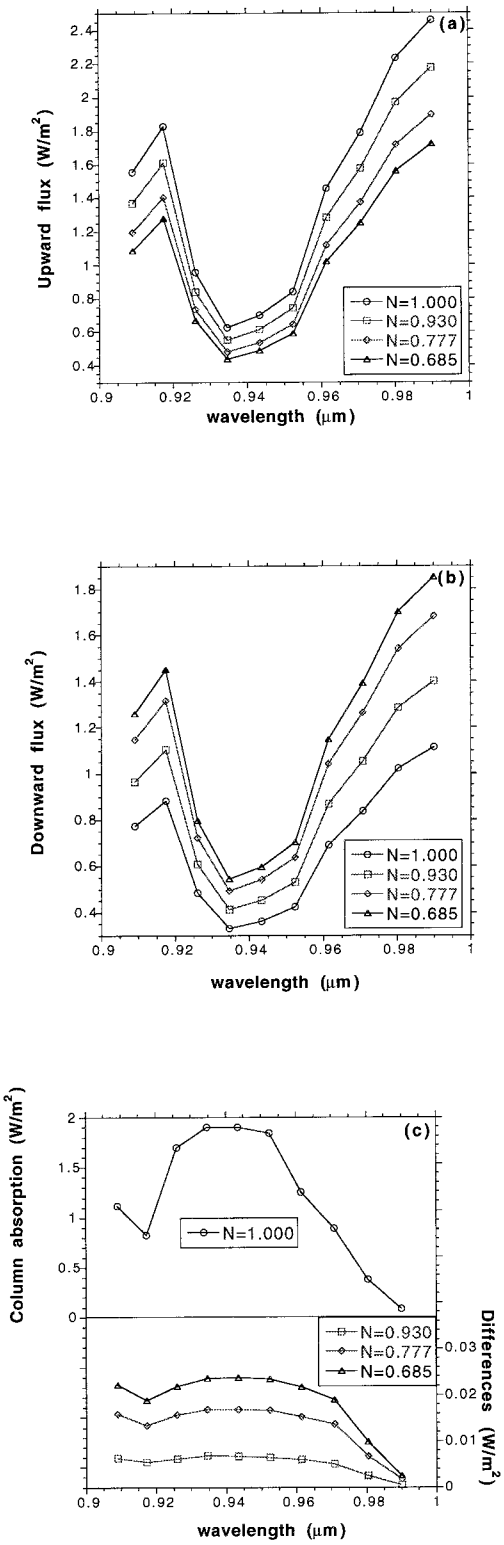

FIG. 9. The effect of cloud fraction for 10 narrow bands. All parameters are as in Fig. 8, MC results only. (a) Upward flux. (b) Downward flux. (c) Column absorption for overcast sky ($N = 1.000$) and differences between overcast sky and broken cloudiness.

deviations, traditionally measured from the simplest (PP) case. Following Cahalan (1994), we define two types of area-averaged biases.

- PP bias determines the changes in radiation fluxes by accounting for the horizontal redistribution of optical depth in cloudy areas (IPA):

$$\Delta F_{\text{model}}(\text{PP}) = F_{\text{IPA}} - F_{\text{PP}}. \tag{19a}$$

- IPA bias determines the changes in radiation fluxes by accounting for photon horizontal transport (MC):

$$\Delta F_{\text{model}}(\text{IPA}) = F_{\text{MC}} - F_{\text{IPA}}. \tag{19b}$$

The total bias is defined as their sum, namely

$$\begin{aligned}\Delta F_{\text{model}}(\text{total}) &= F_{\text{MC}} - F_{\text{PP}} \\ &= \Delta F_{\text{model}}(\text{IPA}) + \Delta F_{\text{model}}(\text{PP}).\end{aligned} \tag{19c}$$

Tables 5a and 5b show PP and IPA biases in up- and downward fluxes as well as in column absorption for both clumpy and bumpy models and four solar zenith angles. Comparing both tables, we see that the PP biases (Table 5a) exceed the IPA ones (Table 5b), at least for up and down fluxes. The PP biases decrease with the increase of solar angle θ_0, not only because of $\cos\theta_0$ in the factor $F_0(\lambda)\cos\theta_0$, where $F_0(\lambda)$ is the solar constant (Table 1), but also in the terms of fractional fluxes, that is, with a unit flux coming to the upper aircraft altitude at 5 km. This follows directly from the Jensen inequality (10a), since with the increase of θ_0, the factor $(1 - g)/2\cos\theta_0$, where g is the phase function asymmetry parameter, increases and the reflectance/transmittance functions become more convex/concave. For the same reason, the PP bias of fractional column absorption decreases as θ_0 increases (Table 5a).

The behavior of the IPA biases is more complex. For both cloud models, the IPA reflectance exceeds the MC one for high-sun elevations, while for low elevations, the MC reflectance is larger (Table 5b). This is consistent with Davis et al.'s (1991) results for zenith sun and is easily understandable. The high-sun photons, penetrating deeper than their low-sun counterparts, bounce back from the thicker neighboring pixels. This effect is more pronounced in the bumpy model. The behavior of transmitted photons is the opposite: the deeper they are in clouds, the less thick (clumpy model) or high (bumpy model) pixels there are around; thus, more of them can be transmitted.

Though IPA bias for reflected or transmitted photons can be either positive or negative, the IPA bias for column absorption is always positive, regardless of the cloud model, solar angle (Table 5b), and cloud fraction (Fig. 8). This means that the horizontal fluxes always *increase* photon path length; hence, 3D radiative effects increase column absorption. Next, IPA absorption bias for the bumpy cloud exceeds the one for the clumpy cloud for all solar angles. The maximal IPA bias is reached at θ_0 between 30° and 45° (Table 5b). The last

TABLE 5a. PP biases for both cloud models. Cloud fraction $N = 0.777$. Both units of flux (W m^{-2}) and dimensionless fractional units are used. To convert flux units to dimensionless ones, divide flux units by a factor of $F_d^a(\theta_0)F_o(\lambda)\cos\theta_0$, where $F_o(\lambda)$ is the solar constant (see Table 1); $F_d^a(0°) = 0.940$, $F_d^a(30°) = 0.934$, $F_d^a(45°) = 0.925$, and $F_d^a(60°) = 0.907$.

		Clumpy model			Bumpy model		
θ_0	Units	Upward	Downward	Absorption	Upward	Downward	Absorption
0°	W m^{-2}	−4.138	4.718	−0.583	−3.918	4.735	−0.820
	(Fract)	(−0.060)	(0.068)	(−0.008)	(−0.057)	(0.069)	(−0.012)
30°	W m^{-2}	−3.431	3.810	−0.378	−3.213	3.806	−0.592
	(Fract)	(−0.058)	(0.064)	(−0.006)	(−0.054)	(0.064)	(−0.010)
45°	W m^{-2}	−2.590	2.803	−0.214	−2.383	2.799	−0.417
	(Fract)	(−0.054)	(0.058)	(−0.004)	(−0.050)	(0.058)	(−0.009)
60°	W m^{-2}	−1.597	1.656	−0.059	−1.477	1.655	−0.178
	(Fract)	(−0.048)	(0.050)	(−0.002)	(−0.044)	(0.050)	(−0.005)

is true for both cloud models and is consistent with results reported by O'Hirok and Gautier (1998).

Finally, comparing both PP and IPA biases, we find that in most cases (for clumpy model and large cloud cover) the negative PP bias in column absorption exceeds the positive IPA bias. As a result, the total bias in (19c) is negative, meaning that the PP absorption is *larger* than its MC counterpart.

The effects of both horizontally homogeneous aerosol and surface albedo (not illustrated here) were explored and found to be rather small on the IPA absorption *bias.* However, their effects on 3D radiative transfer and on column absorption are different: horizontally homogeneous aerosol decreases the IPA absorption bias, whereas nonvanishing surface albedo, as an additional source of photons, increases the difference between MC and IPA.

To roughly estimate the 3D radiative effect on the total broadband absorption, we can use the results of Ramaswamy and Friedenreich's (1991) line-by-line shortwave calculations. The ratio of column absorption in the narrow spectral band of 0.9–1.0 μm to the total broadband shortwave absorption for different types of plane-parallel clouds is typically $\approx$10, with an upper limit of $\approx$20. Thus, if we found that the maximal IPA bias in 0.9–1.0-μm band is 0.35 W m^{-2}, the total *enhancement* of absorption which is due to the 3D radiative effects will likely be around 3–4 W m^{-2}, and almost certainly less than 6 W m^{-2}. This is considerably less than the 15–20 W m^{-2} needed to explain ''enhanced absorption.''

6. Summary

To study the effect of cloud horizontal inhomogeneity on shortwave column absorption, we studied two radically different types of fractal clouds. The first, corresponding more to stratiform clouds, has constant cloud top and base and a fluctuating optical depth—hence, a correspondingly fluctuating extinction coefficient. The second model corresponds more to cumuliform clouds, has identically varying optical depth as the first model but a constant extinction coefficient, and a variable cloud top. For brevity, the first model is labeled ''flat'' or ''clumpy,'' the second ''bumpy.'' Clear-sky gaps are added to both models in an empirical way to simulate the effect of cloud edges. All cloud models (with or without gaps) have the same total amount of liquid water and the same corresponding average optical depth $\langle\tau\rangle = 13$. Maximum cloud optical depth in any pixel is 85 (0.68 cloud fraction); for the flat-but-clumpy model, cloud thickness is 0.3 km, while for the bumpy model, the maximum cloud thickness is $\approx$2 km.

A narrow spectral band from 0.91 to 1.0 μm was selected for the simulations. This band is characterized by insignificant Rayleigh scattering, a large range of transmission, and weak cloud liquid water absorption (ϖ_0 ranges from 0.9998 to 1.0). Thus, the only way to enhance absorption is to increase the total photon path (as opposed to the total number of scatterings).

Three different numerical approaches are used for the radiative transfer calculations:

- the weighted plane-parallel approach that distinguish-

TABLE 5b. IPA biases for both cloud models. All notations are the same as in Table 5a.

		Clumpy model			Bumpy model		
θ_0	Units	Upward	Downward	Absorption	Upward	Downward	Absorption
0°	W m^{-2}	−0.170	0.143	0.028	−0.644	0.343	0.301
	(Fract)	(−0.0025)	(0.0021)	(0.0004)	(−0.0093)	(0.0050)	(0.0044)
30°	W m^{-2}	0.053	−0.137	0.083	−0.296	−0.046	0.342
	(Fract)	(0.0009)	(−0.0023)	(0.0014)	(−0.0050)	(−0.0008)	(0.0058)
45°	W m^{-2}	0.186	−0.281	0.095	−0.143	−0.171	0.314
	(Fract)	(0.0039)	(−0.0058)	(0.0020)	(−0.0030)	(−0.0036)	(0.0065)
60°	W m^{-2}	0.309	−0.374	0.065	0.033	−0.233	0.200
	(Fract)	(0.0093)	(−0.0112)	(0.0019)	(0.0010)	(−0.0070)	(0.0060)

es only between cloudy and clear pixels and assumes all cloudy pixels are identical;
- the independent pixel approximation that goes one step beyond PP by accounting for the horizontal variation of optical depth in cloudy pixels but ignores horizontal fluxes;
- the Monte Carlo method that accounts exactly for horizontal fluxes.

The stability of the domain-averaged results to different realizations of a stochastic cloud model, the level of MC noise, and the connection between point-wise and pixel-average fluxes are evaluated and discussed in appendix B.

The main results of our analysis for the domain averaged and narrowband (0.91–1.0 μm) averaged fluxes are

- Redistribution of cloud liquid water decreases column absorption when horizontal fluxes are ignored; in other words, PP column absorption is always larger than its IPA counterpart. This effect is much more pronounced for the bumpy model than for the clumpy one (Table 5a).
- Horizontal fluxes increase total photon path; MC column absorption is therefore larger than its IPA counterpart. This effect is also more pronounced for the bumpy model than for the clumpy one (Table 5b); horizontal fluxes enhance column absorption by 0.6% for the clumpy model and by up to 2% for the bumpy model (at about $\theta_0 = 45°$) above their IPA levels.
- The total bias (MC $-$ PP) in absorption is negative for high sun and slightly positive for low sun. In other words, the first-order effect of the redistribution of liquid water (PP bias) has a stronger impact on column absorption than 3D effects (IPA bias).

The above conclusion on the IPA bias is valid only for the domain-averaged (50 km) absorption. If we average over 10 km and less, the results become of arbitrary sign and strength (Fig. 5b), depending on many factors including the distribution of cloud gaps and the solar zenith angle. Sometimes, averaging over realizations can compensate for too little spatial averaging. However, this is not always true, since the horizontal distribution of cloud liquid water is essentially nonergodic (Davis et al. 1996).

In addition, we find that the IPA estimate of column absorption for the flat/clumpy model is always larger than its counterpart for the bumpy model. However, the MC column absorption depends rather weakly on the type of model. As a result, bumpiness enhances horizontal fluxes considerably, leaving column absorption almost unchanged.

Finally, decreasing cloud fraction increases the IPA bias. This is due to the number of gaps, hence cloud edge effects in the horizontal fluxes.

Note that the absolute values of the above biases are quite small; they are at most 0.35 W m^{-2}, which is $\approx$2% of the column absorption in 0.91–1.0-μm spectral band. A very rough estimate of a broadband absorption based on the narrowband absorption yields less than $10 \times 0.35 = 3.5$ W m^{-2} enhancement. This is far below the discrepancy between measurements and models reported by Cess et al. (1995) and others. We therefore conclude that 3D effects alone do not explain the discrepancy. This argues for alternate mechanisms for absorption enhancement which may or may not involve clouds (e.g., Li et al. 1997; Crisp 1997).

Acknowledgments. This work was supported by the Environmental Sciences Division of U.S. Department of Energy (under Grant DE-A105-90ER61069 to NASA's Goddard Space Flight Center) as part of the Atmospheric Radiation Measurement (ARM) program. We thank A. Arking, H. Barker, R. Cess, C. Gautier, W. O'Hirok, Z.-Q. Li, R. Pincus, A. Smirnov, and G. Titov for stimulating discussions.

APPENDIX A

Apparent versus Inherent Absorption

In this appendix following Davis et al. (1997), we show that the difference between ''apparent'' absorption A^*, that is, the difference between two net fluxes at different vertical levels, and ''inherent'' column absorption A is given by the photon horizontal transport (see also Titov 1998).

We will use the continuity equation for radiant energy:

$$\nabla \cdot \mathbf{F}(\mathbf{x}) = -\sigma_{\text{abs}}(\mathbf{x}) J(\mathbf{x}), \tag{A1}$$

where $J(\mathbf{x})$ is the total radiance,

$$J(\mathbf{x}) = \int_{4\pi} I(\Omega; \mathbf{x})\, d\Omega, \tag{A2a}$$

and $\mathbf{F}(\mathbf{x}) = (F_x, F_y, F_z)$ is the net radiative flux vector,

$$\mathbf{F}(\mathbf{x}) = \int_{4\pi} \Omega I(\Omega; \mathbf{x})\, d\Omega. \tag{A2b}$$

Radiance $I(\Omega; \mathbf{x})$ obeys the radiative transfer equation (Chandrasekhar 1950)

$$\Omega \cdot \nabla I + \sigma(\mathbf{x}) I(\Omega, \mathbf{x}) = \sigma(\mathbf{x}) \varpi_0 \int_{4\pi} p(\Omega' \to \Omega) I(\Omega', \mathbf{x})\, d\Omega', \tag{A3}$$

where $p(\Omega' \to \Omega)$ is the scattering phase function. [Note that (A1) follows from (A3) after integrating it term-by-term with respect to Ω.] The function $\sigma_{\text{abs}}(\mathbf{x})$ is the monochromatic absorption coefficient,

$$\sigma_{\text{abs}}(\mathbf{x}) = \sigma_{\text{abs}}^{(\text{liquid})}(\mathbf{x}) + \sigma_{\text{abs}}^{(\text{vapor})}(\mathbf{x}). \tag{A4}$$

For simplicity, we assume that $\sigma_{\text{abs}}(\mathbf{x})$ does not vary in the y-direction (hence $\partial F_y/\partial y \equiv 0$), and $\mu_0 F_0 = 1$

where F_0 is the incident flux and $\mu_0 = \cos\theta_0$. Then (A1) can be rewritten as

$$\left(\frac{\partial F_z}{\partial z} + \frac{\partial F_x}{\partial x}\right)(x, z) + \sigma_{\text{abs}}(x, z)J(x, z) = 0. \quad \text{(A5)}$$

Integrating (A5) from z_b to z_a, where $0 < z_b < z_a$ are two aircraft levels above and below clouds, gives

$$\int_{z_b}^{z_a} \left(-\frac{\partial F_z}{\partial z}\right) dz = \int_{z_b}^{z_a} \frac{\partial F_x}{\partial x}\, dz + \int_{z_b}^{z_a} \sigma_{\text{abs}}(x, z)J(x, z)\, dz. \quad \text{(A6)}$$

The left-hand side of (A6) is the ''apparent'' absorption $A^*(x)$ defined as the difference between two net fluxes at z_b and z_a, while the second term on the right-hand side of (A6) is the definition of ''inherent'' or ''true'' column absorption $A(x)$. The remaining term,

$$H(x) = \int_{z_b}^{z_a} \frac{\partial F_x}{\partial x}\, dz, \quad \text{(A7)}$$

determines photon horizontal transport.

The domain-averaged contribution of the horizontal fluxes vanishes exactly:

$$\frac{1}{L}\int_0^L H(x)\, dx = 0 \quad \text{(A8)}$$

with L being the outer scale of our basic cell. (This is because we use cyclical boundary conditions in the horizontal.) Thus, the domain-averaged apparent absorption is equal to the domain-averaged true column absorption, that is,

$$\langle A^* \rangle = \frac{1}{L}\int_0^L A^*(x)\, dx = \frac{1}{L}\int_0^L A(x)\, dx = \langle A \rangle. \quad \text{(A9)}$$

APPENDIX B

Technical Issues

a. Choice of pixel size?

To emulate a large horizontal extension, we have applied cyclical boundary conditions. The number of pixels in the basic cloud element has been set to 1024. The choice of pixel size requires special care.

From one side it cannot be large, because point-wise fluxes measured by ground-based radiometers are approximated by pixel-averaged fluxes. From the other side it cannot be small either, since the below- and especially the above-cloud aircraft get contributions from many identical basic cloud cells which will cancel any variability in the resulting fluxes. Finally, the analysis of cloud liquid water data (Davis et al. 1994, 1996) indicates the scale invariance down to several tens of meters. These factors justify a choice of 50 m for the pixel size. It is significantly less than photon transport

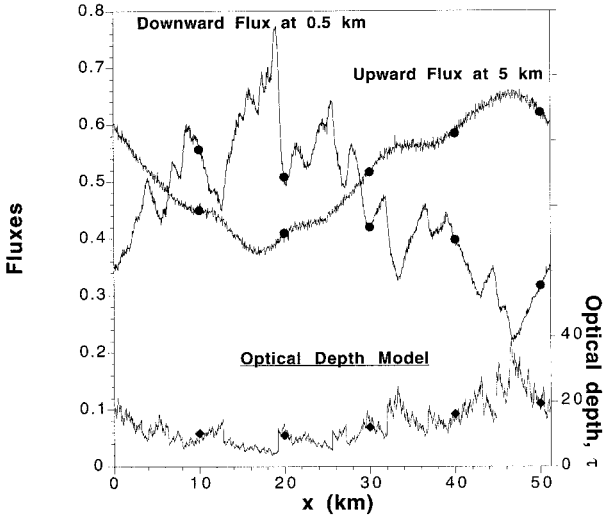

FIG. B1. Forward and backward Monte Carlo for up- and downwelling fluxes. Solar zenith angle $\theta_0 = 30°$, single scattering albedo $\varpi_0 = 1.0$, asymmetry factor $g = 0.84$, no water vapor, and cloud fraction $N = 1.000$. The lower curve is the distribution of cloud optical depth. Black diamonds on it indicate the locations of five point-wise radiometers (10, 20, 30, 40, and 50 km) and the cloud optical depth at these points. Two upper curves correspond to the pixel-averaged up- and downwelling fluxes computed by forward Monte Carlo. Black dots on them indicate the results of backward Monte Carlo for point-wise fluxes.

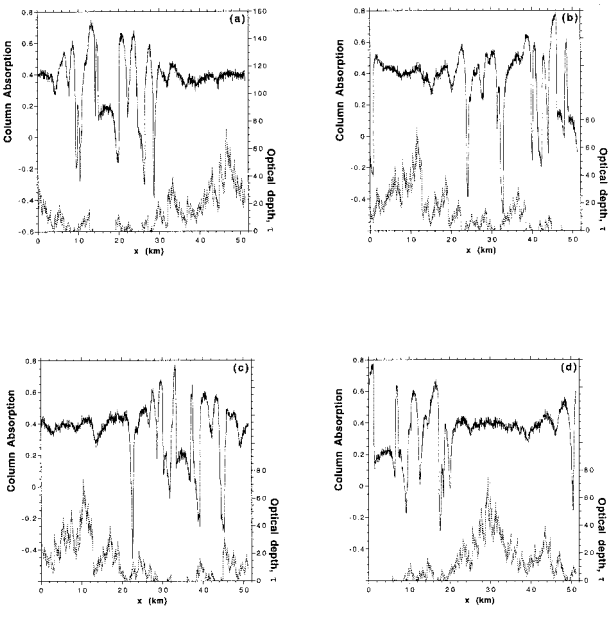

FIG. B2. Monte Carlo apparent absorption fields for different realizations of the clumpy cloud model. Solar zenith angle $\theta_0 = 60°$. All cloud models have approximately the same pdfs corresponding to cloud fraction $N = 0.777$. The domain-averaged MC column absorptions are (a) 0.35367, (b) 0.35375, (c) 0.35375, and (d) 0.35344.

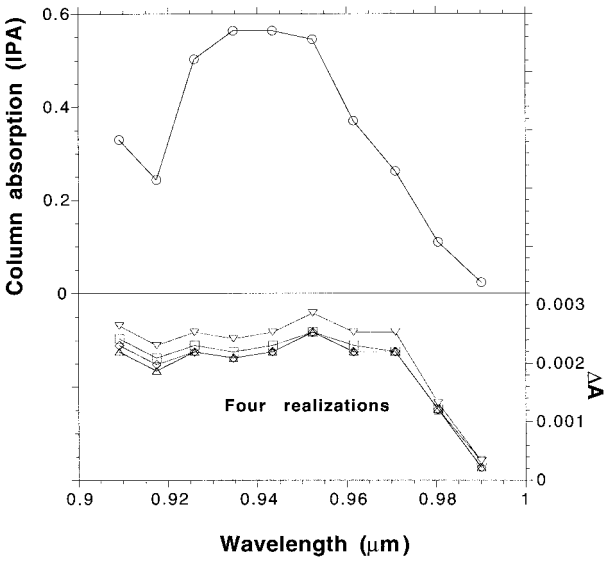

FIG. B3. Domain-averaged column absorption and IPA biases vs wavelength. All parameters are as in Fig. B2. Upper curve corresponds to IPA column absorption. Four lower curves correspond to the IPA bias for four realizations in Fig. B2.

mean free path, $[(1 - g)\langle\sigma\rangle]^{-1} \approx 0.145$ km, if $\langle\tau\rangle = 13$ and $h = 0.3$ km, hence $\langle\sigma\rangle = \langle\tau\rangle/h \approx 43$ km^{-1}, and $g = 0.84$. In this respect, our clouds can be viewed as a stratocumulus deck 0.3-km thick (on average) and $1024 \times 0.05 = 51.2$ km on a side for the basic cell, which is repeated ad infinitum in the x-direction.

b. Local estimates with a ''forward'' Monte Carlo?

To check the validity of the approximation of point-wise fluxes by pixel-averaged fluxes with 50-m pixels, we run both forward and backward MC (Marchuk et al. 1980) codes for the same realization of cloud optical depth. While forward MC provides pixel-averaged fluxes on a pixel-by-pixel basis, backward MC estimates point-wise fluxes in the given locations. Figure B1 illustrates the results for two aircraft-based radiometers, below and above clouds. Agreement is excellent visually, and quantitatively the level of MC noise is about 1% for the forward MC and 0.5% for the backward one.

c. Doing IPA numerically with MC?

For simplicity, all numerical IPA results are computed by MC with huge pixel sizes ($\geq$5000 km) to neglect any interactions between pixels. This incidentally provides us with an illustration of the MC noise in Figs. 4b–c, where IPA results are plotted against optical depth. The width of these curves estimates the level of MC noise (obviously, there is a one-to-one correspondence between optical depth and measured up- and downward fluxes and zero-level noise would yield smooth curves).

d. Different realizations of the cloud model?

One of the advantages of using stochastic models as opposed to deterministic ones is the simple procedure of changing realizations just by picking another random seed. Then a natural question arises: How stable are our results with respect to different realizations of the cloud model? To illustrate this, four different realizations of the clumpy cloud model are used, and respectively, four column absorptions are calculated by MC and IPA.

The domain-averaged IPA results are the same for all realizations, since they have the same pdfs; however, the resulting domain-averaged MC absorptions are not necessarily identical. Indeed, pixel-scale 3D radiative effects depend strongly on the particular horizontal distribution in each realization (Fig. B2). Domain-averaged results are nevertheless very close: 0.3537, 0.3538, 0.3538, and 0.3534. Figure B3 shows IPA column absorption together with four IPA biases plotted against a wavelength between 0.9 and 1.0 μm. As in the case study in the main text, the IPA column absorption is always smaller ($\approx$0.3517); so IPA biases are positive for all four realizations and all 10 narrow spectral bands.

To conclude, although the domain-averaged column absorptions for different realizations of cloud models are not identical, they are close enough; the difference is less than 0.5%, while the MC domain-averaged errors—checked using IPA—are less than 0.1%. Thus, the results reported in this paper obtained by using just one realization of a cloud model can be viewed as robust.

REFERENCES

Ackerman, S. A., and S. K. Cox, 1981: Aircraft observations of the shortwave fractional absorptance of non-homogeneous clouds. *J. Appl. Meteor.,* **20,** 1510–1515.

Arking, A., 1996: Absorption of solar energy in the atmosphere: Discrepancy between model and observations. *Science,* **273,** 779–782.

Barker, H., 1995: A spectral analysis of albedo and bidirectional reflectances for inhomogeneous clouds. *Remote Sens. Environ.,* **54,** 113–120.

——, 1996: A parameterization for computing grid-averaged solar fluxes for inhomogeneous marine boundary layer clouds. Part I: Methodology and homogeneous biases. *J. Atmos. Sci.,* **53,** 2289–2303.

——, and J. A. Davies, 1992: Cumulus cloud radiative properties and the characteristics of satellite radiance wavenumber spectra. *Remote Sens. Environ.,* **42,** 51–64.

Byrne, R. N., R. C. Somerville, and B. Subasilar, 1996: Broken-cloud enhancement of solar radiation absorption, *J. Atmos. Sci.,* **53,** 878–886.

Cahalan, R. F., 1994: Bounded cascade clouds: Albedo and effective thickness. *Nonlinear Processes Geophys.,* **1,** 156–167.

——, and J. B. Snider, 1989: Marine stratocumulus structure during FIRE. *Remote Sens. Environ.,* **28,** 95–107.

——, W. Ridgway, W. J. Wiscombe, T. L. Bell, and J. B. Snider, 1994: The albedo of fractal stratocumulus clouds. *J. Atmos. Sci.,* **51,** 2434–2455.

——, D. Silberstein, and J. B. Snider, 1995: Liquid water path and plane-parallel albedo bias during ASTEX. *J. Atmos. Sci.,* **52,** 3002–3012.

Cess, R. D., and Coauthors, 1995: Absorption of solar radiation by clouds: Observations versus models. *Science,* **267,** 496–499.

——, M. H. Zhang, Y. Zhou, X. Jing, and V. Dvortsov, 1996: Absorption of solar radiation by clouds: Interpretations of satellite, surface, and aircraft measurements. *J. Geophys. Res.,* **101,** 23 299–23 309.

Chandrasekhar, S., 1950: *Radiative Transfer*. Oxford University Press, Reprint, Dover, 1960, 393 pp.

Chou, M.-D., A. Arking, J. Otterman, and W. Ridgway, 1995: The effect of clouds on atmospheric absorption of solar radiation. *Geophys. Res. Lett.,* **22,** 1885–1888.

Crisp, D., 1997: Absorption of sunlight by water wapor in cloudy conditions: A partial explanation for the cloud absorption anomaly. *Geophys. Res. Lett.,* **24,** 571–574.

Davis, A., S. Lovejoy, and D. Schertzer, 1991: Discrete angle radiative transfer in a multifractal medium. *S.P.I.E. Proceedings,* V. V. Varadan, Ed., 37–59.

——, A. Marshak, W. Wiscombe, and R. Cahalan, 1994: Multifractal characterizations of non-stationarity and intermittency in geophysical fields, observed, retrieved or simulated. *J. Geophys. Res.,* **99,** 8055–8072.

——, ——, ——, and ——, 1996: Multifractal characterizations of intermittency in nonstationary geophysical signals and fields. A model-based perspective on ergodicity issues illustrated with cloud data. *Current Topics in Nonstationary Analysis,* G. Trevino, J. Hardin, B. Douglas, and E. Andreas, Eds., World-Scientific, 97–158.

——, ——, W. J. Wiscombe, and R. F. Cahalan, 1997: Evidence for net horizontal radiative fluxes in marine stratocumulus. *IRS'96: Current Problems in Atmospheric Radiation,* W. L. Smith and K. Stamnes, Eds., Deepak, 809–812.

Ellingson, R. G., J. Ellis, and S. Fels, 1991: The intercomparison of radiation codes used in climate models: Long wave results. *J. Geophys. Res.,* **96,** 8929–8953.

Fouquart, Y., J. C. Buriez, and M. Herman, 1990: The influence of clouds on radiation: A climate-modeling perspective. *Rev. Geophys.,* **28,** 145–166.

——, B. Bonnel, and V. Ramaswamy, 1991: Intercomparing shortwave radiation codes for climate studies. *J. Geophys. Res.,* **96,** 8955–8968.

Harshvardhan, W. Ridgway, V. Ramaswamy, S. M. Freidenreich, and M. Batley, 1996: Solar absorption in cloudy atmosphere. Preprints, *Seventh Symp. on Global Change Studies,* Atlanta, GA, Amer. Meteor. Soc., 127–134.

Hayasaka, T., N. Kikushi, and M. Tanaka, 1995: Absorption of solar radiation by stratocumulus clouds: Aircraft measurements and theoretical calculations. *J. Appl. Meteor.,* **34,** 1047–1055.

Hermann, G., and R. Goody, 1976: Formation and persistence of summertime Arctic stratus clouds. *J. Atmos. Sci.,* **33,** 1537–1553.

King, M. D., L. F. Radke, and P. V. Hobbs, 1990: Determination of the spectral absorption of solar radiation by marine stratocumulus clouds from airborne measurements within clouds. *J. Atmos Sci.,* **47,** 894–907.

Lacis, A. A., and V. Oinas, 1991: A description of the correlated *k*-distribution method for modeling nongray gaseous absorption, thermal emission, and multiple scattering in vertically inhomogeneous atmospheres. *J. Geophys. Res.,* **96,** 9027–9063.

Li, Z.-Q., L. Moreau, and A. Arking, 1997: On solar energy disposition: A perspective from observation and modeling. *Bull. Amer. Meteor. Soc.,* **78,** 53–70.

Marchuk, G., G. Mikhailov, M. Nazaraliev, R. Darbinjan, B. Kargin, and B. Elepov, 1980: *The Monte Carlo Methods in Atmospheric Optics.* Springer-Verlag, 208 pp.

Marshak, A., A. Davis, R. Cahalan, and W. Wiscombe, 1994: Bounded cascade models as non-stationary multifractals. *Phys. Rev. E.,* **49,** 55–69.

——, ——, and W. Wiscombe, 1995: Radiation smoothing in fractal clouds. *J. Geophys. Res.,* **100,** 26 247–26 261.

——, ——, W. J. Wiscombe, and R. F. Cahalan, 1997a: The effect of horizontal fluxes on cloud absorption estimates based on simulated two-aircraft measurements of fractal clouds. *IRS'96: Current Problems in Atmospheric Radiation,* W. L. Smith and K. Stamnes, Eds., Deepak, 415–418.

——, ——, ——, and ——, 1997b: Inhomogeneity effects on cloud shortwave absorption measurements: Two-aircraft simulations. *J. Geophys. Res.,* **102,** 16 619–16 637.

O'Hirok, W., and C. Gautier, 1998: A three-dimensional radiative transfer model to investigate solar radiation within cloudy atmosphere. Part I: Spatial effects. *J. Atmos. Sci.,* in press.

Pilewskie, P., and F. P. Valero, 1995: Direct observations of excess solar absorption by clouds. *Science,* **267,** 1626–1629.

Pólya, G., and G. Szegö, 1964: *Aufgaben und Lehrsätze aus der Analysis.* Vol. 2. Springer-Verlag, 391 pp.

Ramanathan, V., B. Subasilar, G. J. Zhang, W. Conant, R. D. Cess, J. T. Kiehl, G. Grassl, and L. Shi, 1995: Warm pool heat budget and short-wave cloud forcing: A missing physics? *Science,* **267,** 499–503.

Ramaswamy, V., and S. M. Friedenreich, 1991: Solar radiative line-by-line determination of water vapor absorption and water extinction in inhomogeneous atmospheres. *J. Geophys. Res.,* **96,** 9133–9157.

Reynolds, D. W., T. H. Vonder Haar, and S. K. Cox, 1975: The effect of solar radiation absorption in the tropical atmosphere. *J. Appl. Meteor.,* **14,** 433–444.

Stephens, G. L., 1978a: Radiation profile in extended water clouds. I: Theory. *J. Atmos. Sci.,* **35,** 2111–2122.

——, 1978b: Radiation profile in extended water clouds. II: Parameterization schemes. *J. Atmos. Sci.,* **35,** 2123–2132.

——, 1988: Radiative transfer through arbitrarily shaped media. Part II: Group theory and closures. *J. Atmos. Sci.,* **45,** 1837–1848.

——, and S.-C. Tsay, 1990: On the cloud absorption anomaly. *Quart J. Roy Meteor. Soc.,* **116,** 671–704.

Tiedke, M., 1996: An extension of cloud-radiation parameterization in the ECMWF model: The representation of subgrid-scale variations in optical depth. *Mon. Wea. Rev.,* **124,** 745–750.

Titov, G. A., 1998: Radiative horizontal transport and absorption by stratocumulus clouds. *J. Atmos. Sci.,* in press.

van de Hulst, H. C., 1980: *Multiple Light Scattering (Tables, Formulas, and Applications).* Vol. 2. Academic Press, 739 pp.